Experimental Correlation of the Role of Synthesized Biochar on Thermal, Morphological, and Crystalline Properties of Coagulation Processed poly(1,4-Phenylene Sulfide) Nanocomposites

Zaib Un Nisa *, Lee Kean Chuan, Beh Hoe Guan, Faiz Ahmed, Saba Ayub

Posted Date: 16 March 2023

doi: 10.20944/preprints202303.0303.v1

Keywords: Synthesis; characterization; carbonization; coagulation; bio char; nanocarbon; morphological

Article

Experimental Correlation of the Role of Synthesized Biochar on Thermal, Morphological, and Crystalline Properties of Coagulation Processed Poly(1,4-Phenylene Sulfide) Nanocomposites

Zaib un Nisa [1] *, Lee Kean Chuan [1], Beh Hoe Guan [1], Faiz Ahmad [2] and Saba Ayub [1]

1. Department of Fundamental and Applied Sciences, Universiti Teknologi PETRONAS, Seri Iskandar 32610 Perak, Malaysia2610 Perak, Malaysia
2 Department of Mechanical Engineering, Universiti Teknologi PETRONAS, Seri Iskandar 32610 Perak, Malaysia2610 Perak, Malaysia
* Correspondence: zaib_20001001@utp.edu.my

Abstract This work aimed to study the thermal and crystalline properties of poly (1,4-phenylene sulfide)@carbon char nanocomposites. Coagulation-processed nanocomposites of polyphenylene sulfide were prepared using synthesized mesoporous nanocarbon of coconut shell as reinforcement. The mesoporous reinforcement was synthesized using a facile carbonization method. The investigation of the properties of nanocarbon was done by SAP, XRD, and FESEM analysis. The research was further propagated via the synthesis of nanocomposite by the addition of characterized nanofiller into poly (1,4-phenylene sulfide) at five different combinations. The coagulation method was utilized for the nanocomposite formation. The obtained nanocomposite was analyzed using FTIR, TGA, DSC, and FESEM analysis. The BET surface area and average pore volume of bio-carbon prepared from coconut shell residue were calculated to be 1517 m^2/g and 2.51 nm respectively. The addition of nanocarbon to poly (1,4-phenylene sulfide) has led to an increase in thermal stability and crystallinity up to 6% loading of filler. The minimum achievable glass transition temperature is for 6 % doping of filler into the polymer matrix. It was established that the thermal, morphological, and crystalline properties have been tailored by synthesizing their nanocomposites with mesoporous bio-nanocarbon obtained from coconut shells. There is decline in glass transition temperature from 126 ^oC to 117 ^oC using 6% filler. The crystallinity values are decreasing continuously with the filler mixing exhibiting the incorporation of flexibility in polymer. So, the loading of filler into poly (1,4-phenylene sulfide) can be optimized to enhance its thermoplastic properties for surface applications.

Keywords: synthesis; characterization; carbonization; coagulation; bio char; nanocarbon; morphological

1. INTRODUCTION

The carbon products obtained from industrial sources has been used as filler in various polymers [1–3]. It has been extensively practiced in industrial sectors to advance the routine properties of polymeric products [4–6]. There has been a dynamic study in industrial and academic fields to study composites and nanocomposites of polymers. Polymeric composites have proven as a major and unremarkable endeavor. The major technical and commercial interest lies in the ubiquitous existence of properties in consumer products. Usually, the polymers modified with carbon products have been investigated for their thermal, conductive, thermoelectric, tensile, mechanical, corrosion, and erosive properties [7–10].

The production of biochar (BC) from agricultural waste is the leading and cheapest source for the production of nanocarbon as an industrial product with a predicted yearly production of fifteen metric tons by 2025 [11]. BC is fundamentally produced from the carbonization of carbon resources such as biomass, fossil fuels, and biofuels [12]. Thus, to achieve large-scale productivity, low-cost raw material, and inexpensive products with required properties, BC can be seen to be an appealing choice [13,14].

 doi:10.20944/preprints202303.0303.v1

It is a known fact that carbon-based materials like carbon black, chars, or activated carbon have demonstrated fine pore size development than wood-based carbon products. The majority of the pore volume has shown a radius of < 1 nm in the case of coconut shells, while carbon material originating from wood has a significant number of macropores and mesopores [15,16]. A survey was performed on various agricultural by-products like almond shells and seeds of peach, grape, cherry, apricot, and palm with the conclusion that the botanical origin of the family of the selected material also affects the distribution of pore size [17,18]. BC specifically obtained from coconut shells as a bio-carbon source has the potential for substituting the conventional thermoset filler in wear applications due to their high strength, low density, hardness, abrasion resistance, and modulus properties [19,20].

The tailoring in inbuilt characteristics and achievement of required characters of a matrix is usually accomplished by using fillers poly(1,4-phenylene sulfide) (PPS) is the most extensively utilized semicrystalline polymer. It retains superior thermal, chemical, mechanical, antiaging, flame resistant, water resistant, low thermal expansion coefficient, and exceptional friction properties [21,22]. Surface protection is one of the major requirements of industries using high-temperature conditions. The PPS has been successfully employed as a protective coating because of superior melt temperature, good chemicals, and excellent abrasive resistance. PPS is a high-performance thermoplastic so its high-performance thermoplastic composites are taking a progressively significant role in thermoplastic applications. The benefits include the properties such as elevated impact resistance, toughness, better chemical and corrosion endurance, easy processing, indefinite shelf lifespan of the prepregs, and the ability to get recycled [23,24].

In the category of carbon-based composites of PPS investigation has been carried out using glass fiber (GF), carbon fiber (CF), metal oxides, graphene, Mxene, short carbon fibers (SCFs), nanodiamonds (NDs), and graphene oxide (GO). Systematic evaluation of behavioral isothermal and non-isothermal crystallization of PPS modified with short glass fiber has been done by different models. Detail is available on the crystallization evolution, dynamic mechanical properties, along with aging effects using heat treatment [25]. The PPS and CF-reinforced composites have been investigated for thermomechanical, fracture resistance, and tribological properties [26]. Short carbon fibers graphene oxide, and nanodiamonds (NDs) based composites of PPS have been reported for their ability to be utilized in membranes, friction reduction, and wear applications [27]. Its conductive polymer composites have been discovered as feasible replacements for electrolytic membranes of fuel cells and bipolar plates [28].

Research findings on the use of activated nanocarbon in various material manufacturing are still on way because of its ability in renewable energy harvesting [29,30], and environmental applications especially focusing on global challenges on clean energy, sensors [31], dielectric and EMI applications [32], high-performance batteries [33], electrochemical energy storage, and environmental remediation [34,35]. The addition of BC to elastomeric materials has been studied in many industrial applications [36,37]. In current research seeing the easy tailorability and modifiable properties of PPS for many useful applications, its undiscovered biochar-based composites (PPS@BC) were synthesized. BC was synthesized from raw coconut shells. As a high-performance engineering polymer thermal and crystallization properties of PPS are shown to be affected by the percentage of blending, technique of synthesis, and nature of reinforcement [29,38].

Herein study was conducted to explore the thermal, morphological, and crystalline properties of the PPS@BC composites. Composites were made using the coagulation protocol. The investigation was done by loading different percentages of synthesized BC to the PPS matrix and variation in properties was studied.

2. EXPERIMENTAL

2.1. Raw Materials

PPS powder (Average Mn~10,000 g mol $^{-1}$, density= 1.36 g/mL at 25 °C) was supplied by Sigma-Aldrich USA, NMP reagent grade was purchased from Supelco Germany (b.p. = 202 °C), Methanol obtained from Friendemann Schmidt sdn bhd (b.p. = 64.9 °C) and used as received. The mesoporous

Preprints (www.preprints.org) | NOT PEER-REVIEWED | Posted: 16 March 2023 doi:10.20944/preprints202303.0303.v1

biochar (BC) was synthesized from the coconut shell and characterized in the laboratory using the following carbonization technique. The schematic diagram for the workflow is presented in Figure 1.

2.2. Synthesis of biochar BC

After being washed with distilled water coconut shells were dried at 80 °C in an oven. The dried shells were granulated using a granulator to obtain smaller grains. The prepared grains of the coconut shells were treated in a tube furnace to bring out the carbonization as follows [39].

The ceramic boat was loaded with grains of coconut shells and treated thermally in a tube furnace (PROTHERM model: PTF 12/75/800, tube type: C610) having dimensions of DxWxH 635x 850x400. The carbonization was carried out under nitrogen at 700 °C with a 10 °C/min increase in temperature. Following thermal treatment for two hours, the carbonized product was allowed to come at room temperature with an annealing time of eight hours. The thermally degraded product was further ground in dry form using a laboratory blender (WARING, Model No. HGBTWTG4 to get powder. The obtained BC was further sieved with 3 U.S. mesh to obtain a fine powder.

2.3. Physical activation of BC

The synthesized biochar was physically activated at a temperature of 700 °C in an atmosphere of carbon dioxide. The flow of carbon dioxide was set to 100 ml/min. The heating temperature and gas flow remained constant for six hours. After the physical activation, the product was brought to room temperature under nitrogen [40].

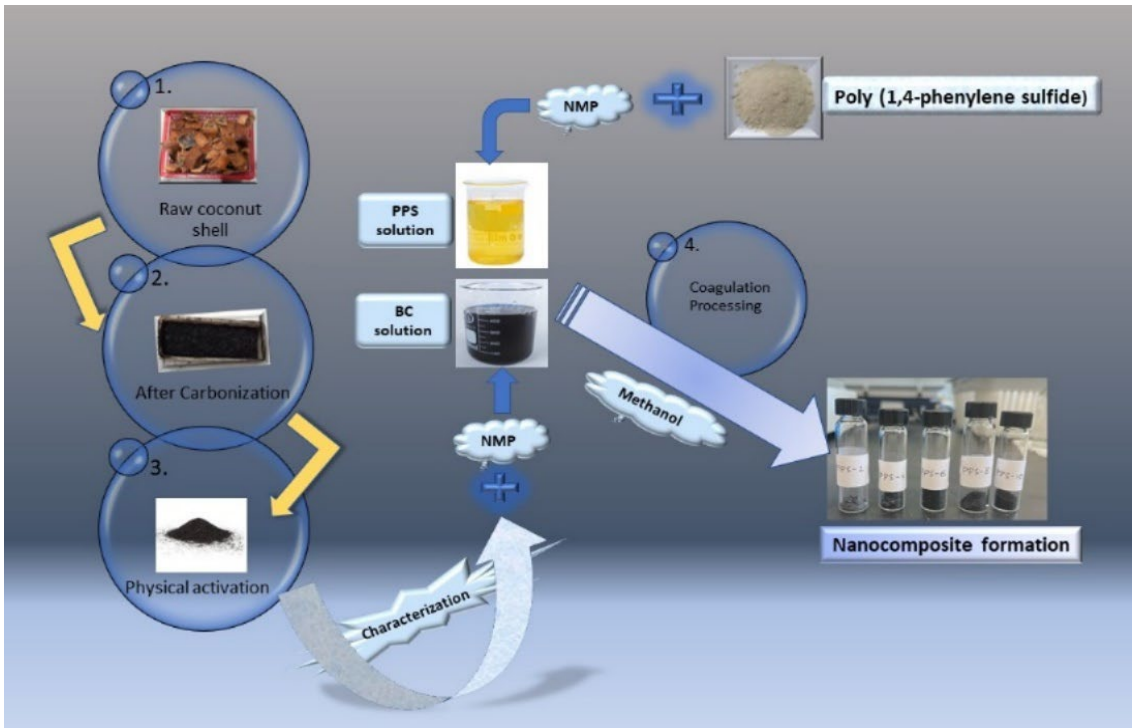

Figure 1. Schematic flow of the experimental workup.

2.4. Synthesis of PPS@BC nanocomposites using the coagulation method

PPS was dissolved in N-Methyl-2-pyrrolidone (NMP) at 350 °C using a hot plate until a clear solution was obtained. Synthesized mesoporous BC was evenly dispersed as filler in NMP using ultrasonication for 30 minutes in a separate beaker. The two solutions were mixed with five different compositions of 2%, 4%, 6%, 8%, and 10% of mesoporous nanofiller. Homogenous dispersion of BC was achieved by ultrasonication of the mixture for 30 minutes. 50 ml methanol was added to the reaction mixture with continuous stirring to obtain the flocculates. The reaction mixture was further

Preprints (www.preprints.org) | NOT PEER-REVIEWED | Posted: 16 March 2023 doi:10.20944/preprints202303.0303.v1

ultrasonicated for another 10 minutes. After filtration of the coagulated nanocomposite, the product was dried at 80 °C under a vacuum.

3. CHARACTERIZATION TECHNIQUES

3.1. Characterization of BC

The characterization techniques utilized to study morphology, elemental identification, phase composition, crystallinity, particle size, dimension, and specific surface area of BC were BET, XRD, and SEM with EDS.

Brunauer, Emmet, and Teller (BET) evaluations were made on Micromeritics (ASAP 2020) instrument and the specific surface area of the product was measured by N_2 adsorption. Analysis of X-ray Powder Diffraction (XRD) instrument was performed on (Bruker, AXS, D8 advance) using Cu Kα (λ_1 = 1.54056 °A & λ_2 = 1.5444 °A with a ratio of λ_2/λ_1 = 0.5) radiation source (45 kV & 40 mA) in continuous scanning mode. The samples were examined at a scanning speed of 1° min^{-1} from 10° to 100° on a 2θ scale. The Carl Zeiss (Supra 55vp) instrument was utilized to achieve field-emission scanning electron microscope (FESEM) images.

3.2. Characterization of PPS@BC composites

Four characterization techniques were utilized to analyze the structural, thermal, and morphological properties of PPS@BC nanocomposites. The Fourier transform infrared spectra were recorded on an FTIR instrument, Perkin Elmer (FTIR Frontier) using KBr solid-state analysis. Thermal characterization was carried out using Perkin Elmer (STA6000) thermobalance, at a heating rate of 10 °C/min under an N_2 atmosphere up to a maximum temperature of 600 °C. Differential Scanning Calorimetry (DSC) analysis was performed under N_2 using Perkin Elmer (Pyris-1) instrument. The samples were heated from 50-800 °C for a complete cycle at a heating rate of 10 °C/ min. The field-emission scanning electron microscope (FESEM) imaging was obtained using Carl Zeiss (Supra 55vp) instrument.

4. RESULTS AND DISCUSSION

4.1. Surface morphology and composition of BC

Field emission scanning electron microscopy (FESEM) imaging with energy-dispersive X-ray spectroscopy (EDS), is a valuable analytical tool for surface study in terms of morphology and composition using EDS. The observed images of synthesized nanocarbon at different magnifications captured at an acceleration potential of 5 to 200 kV are presented in Figure 2. The obtained images expose the porous morphology of the carbonized coconut shell product. This acknowledges the fact that carbonized product of coconut shell at given conditions is feasible for having nanocarbon with better surface area, which later has been supported by SAP results. So, carbonization temperature and time for the physical activation of material have proven a crucial role in the carbonization process.

The back scattered electron (BSE) image and determined composition by weight using EDS analysis is presented in Figure 3. The prepared BC contains 90.2 % carbon 9.5 % oxygen and 0.3 % potassium by weight fraction as listed in Table 1. So, most of the ingredients of the coconut shell have been degraded well and carbonized coconut shell residue in the form of required biochar is containing a copious amount of carbon.

Preprints (www.preprints.org) | NOT PEER-REVIEWED | Posted: 16 March 2023 doi:10.20944/preprints202303.0303.v1

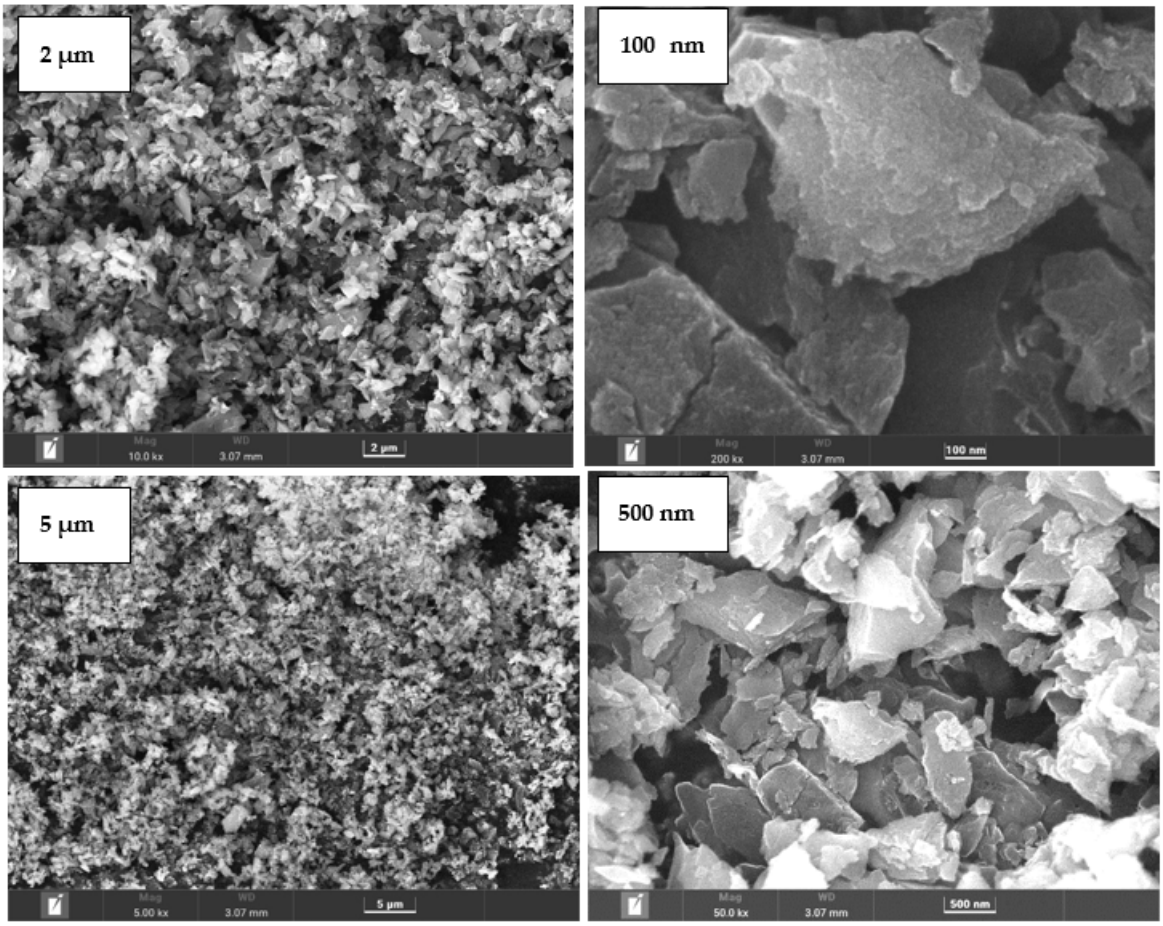

Figure 2. FESEM overview of BC at different magnifications.

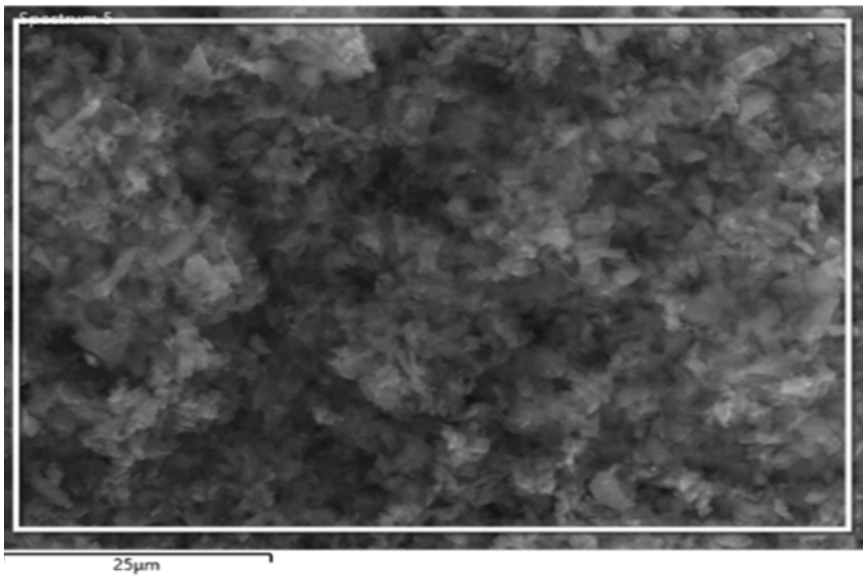

Figure 3. BSE image of BC.

Preprints (www.preprints.org) | NOT PEER-REVIEWED | Posted: 16 March 2023 doi:10.20944/preprints202303.0303.v1

Table 1. EDS composition of BC.

Sample	Carbon (wt %)	Oxygen (wt %)	Potassium (wt %)
BC	90.2	9.5	0.3

4.2. SAP analysis of BC

Parameters related to the surface of a material can be used for physical adsorption phe-nomena. Brunauer-Emmett-Teller's (BET) theory is used to explain the physical adsorption of gas molecules on a solid surface. This analytical technique provides useful information for the measurement of the specific surface area of materials. The underlying phenomenon is the physical adsorption of gas molecules on the surface of material via London dispersion forces. The International Union of Pure and Applied Chemistry (IUPAC) has recognized that absorbent surfaces can give rise to five conventional types of isotherms [31]. SAP study of the product presented smooth type III isotherm according to IUPAC classification predicting stronger adsorbent adsorbate interactions.

The adsorbate dissemination into a material will is utilized in SAP analysis. The volume, size, and diameter of pores are directly related to the adsorption capacity of a surface. This selectivity in an appropriate structure with requisite pore considerations is of key interest for a particular application [41]. The selection of raw material, processing conditions, and adequate activation surface play a key role in pore development [42,43].

Table 2. SAP parameters of BC.

Sample	Specific surface area (S_{BET})	Langmuir surface area (S_L)	Average pore diameter (D)
BC	1517 m^2/g	2175 m^2/g	2.51 nm

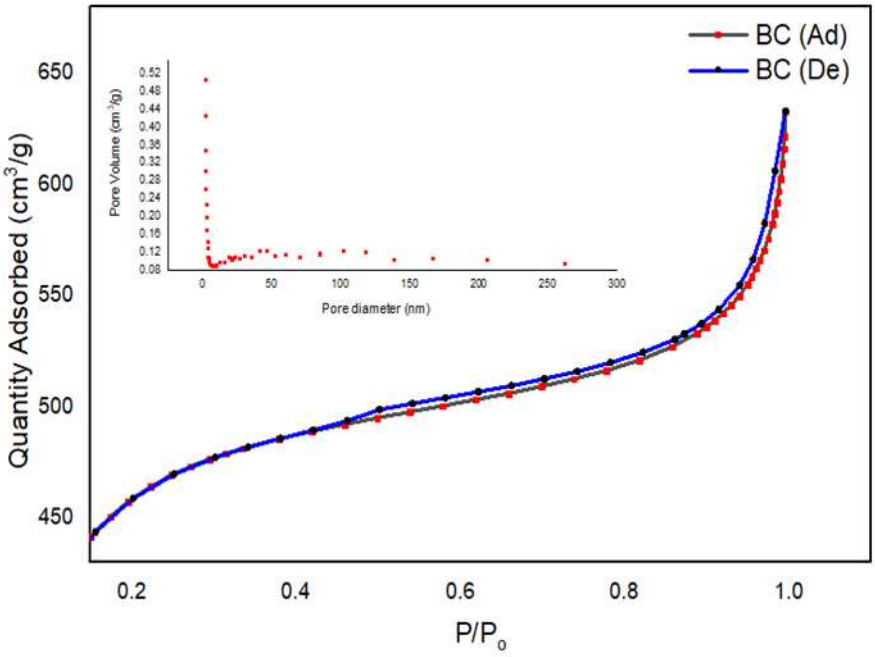

Figure 4. Isotherm linear plots and size distribution analysis of BC at STP.

The achieved isotherm linear curve including size distribution analysis of BC at STP is given in Figure 4. The initial part of the linear isotherm plot of the isotherm for BC represents the saturation of the pores with the nitrogen gas used for analysis. This is shown as the BC adsorption curve (ad). The second curve De is abbreviated for the desorption analysis of BC. The slope of the plateau at relatively high pressure depicts the multilayer adsorption of absorbate on the porous BC surface [36]. The details of measured SAP parameters are given in Table 2. The average pore diameter was

Preprints (www.preprints.org) | NOT PEER-REVIEWED | Posted: 16 March 2023 doi:10.20944/preprints202303.0303.v1

calculated to be in nano size (2.51 nm) with specific surface area (SBET), and Langmuir surface (SL) area values of 1517 m^2/g and 2175 m^2/g respectively. In literature, char materials are usually reported with chemical activation. In a review of the chemical activation of agricultural residues, the SBET is reported with a range of 0.1-1718 m^2/g [44]. In the current study, the area achieved is comparable to the maximum achieved value even using facile processing parameters.

4.3. X-ray diffraction analysis of BC

X-Ray diffraction analysis (XRD) is known as a useful nondestructive technique to obtain comprehensive knowledge about the crystal structure, chemical composition, crystallographic parameters, and physical properties of a material [44,45]. Carbon is made up of a combination of heterogeneous atoms and their thickness can vary from monolayer to multilayer arrangement so there is a small change in crystallographic parameters depending on the processing parameters and raw material. The obtained XRD spectra for BC are given in Figure 5. The reported structural parameters of BC in terms of interplanar spacing (d_{hkl}), full-width half maximum (FWHM), crystallite size (L_c), lateral size (L_a), no of layers (N), dislocation density (δ), microstrain (ε), packing density (ϱ), and crystallinity index were calculated using the method from the literature [46]. The XRD spectral pattern revealed two strong Braggs peaks associated with reflections from (002) and (10) planes. The calculated peak position of BC on the 2θ scale in degrees is presented in Table 3. The major peak due to reflection from the (002) plane is located at 24.8° on the 2θ scale. The relatively smaller peak at 40.7° on the 2θ scale is because of two-dimensional reflection from the (10) plane. The calculated microstructural parameters for the synthesized BC are tabulated in Table 4. It is supported by the reported results that observed microstructural parameters are showing small lattice dimensions and degree of graphitization [47–49]. The percent crystallinity of BC was calculated using the following formula (1).

Crystallinity Index (%) = (I crystalline/I total) * 100 (1)

The intensity ratio of the crystalline peak was related to the amorphous peak using their respective mass ratios and the degree of crystallinity was accomplished [46]. The calculated crystallinity index of 53.07 % was observed for BC.

Table 3. Peak position (°) of BC on the 2θ scale determined from the XRD pattern.

Sample	Plane (002)	Plane (10)
BC	28.4	40.7

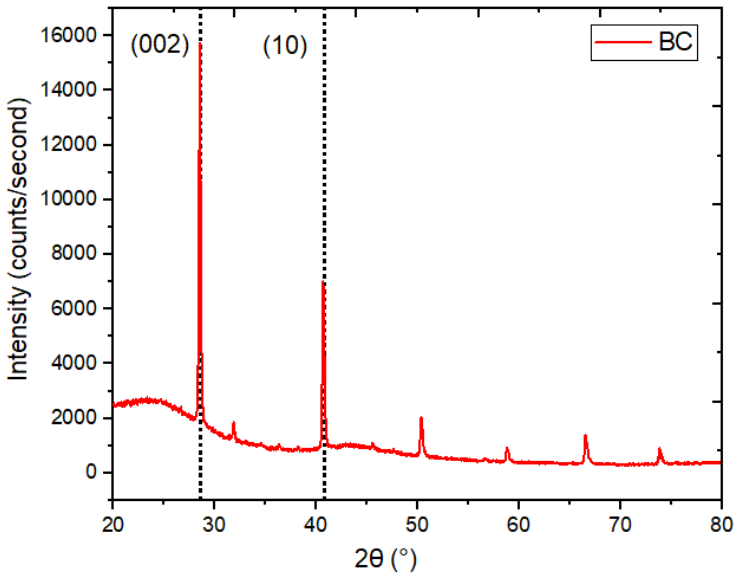

Figure 5. XRD spectral pattern of BC.

Preprints (www.preprints.org) | NOT PEER-REVIEWED | Posted: 16 March 2023 doi:10.20944/preprints202303.0303.v1

Table 4. Structural information of BC determined from XRD patterns.

Sample	d_{002} (Å)	FWHM	L_c (nm)	L_a (nm)	N (Items)	δ (nm^{-2})	ε (x 10^{-3})	ϱ (g/cm^3)	Crystallinity Index (%)
BC	3.140	0.195	42.024	90.585	13.383	0.566	3.362	0.243	53.077

4.4. FTIR interpretation of PPS@BC nanocomposite

PPS@BC nanocomposites were synthesized using the coagulation technique. The coagulant used was methanol and the neat polymer was also analyzed along with synthesized nanocomposites. The samples were investigated from 4000-550 cm^{-1} and the results are given in Table 5. The structure of PPS most likely resembles para-substituted benzene; however, it is challenging to assign the individual modes.

The obtained spectra are presented in Figure 6. In spectra, the highly noticeable peaks are due to symmetric and asymmetric benzene ring stretch [50]. These appear in the region from 1600 cm^{-1} to 1300 cm^{-1}. The peak assigned due to the symmetric stretch is sharp compared with a wide peak of the asymmetric stretch. These peaks are shifted to higher frequency values in the case of nanocomposites compared with neat polymers. Aromatic C-H stretching vibrations are not very prominent and showed a small broad peak in the region of 2300 cm^{-1}.

The carbon atom of the substituted benzene ring linked with sulfur reflected a wide band above 1800 cm^{-1}. The out-of-plane C-H vibrations presented distinctive medium peaks in the region from 807-811 cm^{-1} [51]. The characteristic C-S stretching vibrations of the benzene ring are present in lower frequency regions above 450 cm^{-1}. Variation in band intensity is noticed as synthesized filler is added into the neat PPS polymer. Such changes may be due to changes in the symmetry and crystallinity of the matrix upon the addition of synthesized nanocarbon.

Table 5. FTIR data of PPS@BC nanocomposites.

Samples	Wavenumber (cm^{-1})						
	O-H (stret)	C-H (stret)	Benz ring (sym stretch)	Benz ring (asym stret)	C-S (aliph stret)	C-H (out of plane)	Benz ring (sym ring-S stretch)
PPS	-	2373 (w)	1454 (s)	1382 (w)	1087 (w)	807 (m)	476 (m)
PPS-2	3433 (w)	2333 (w)	1647	1462 (w)	1082 (w)	811 (m)	469 (m)
PPS-4	3433 (s)	2365 (w)	1652 (s)	1468 (w)	1087 (w)	817 (m)	475 (m)
PPS-6	3433 (s)	2341 (w)	1657 (s)	1468 (w)	1089 (w)	817 (m)	480 (m)
PPS-8	3433 (s)	2398 (w)	1657 (s)	1468 (w)	1089 (w)	811 (m)	478 (m)
PPS-10	3433 (s)	2364 (w)	1652 (s)	1468 (w)	1084 (w)	811 (m)	475 (m)

aliph= aliphatic, stret = stretching, sym= symmetric, asym= asymmetric, Benz = Benzene, w = Weak, s = Sharp, m = Medium

Preprints (www.preprints.org) | NOT PEER-REVIEWED | Posted: 16 March 2023 doi:10.20944/preprints202303.0303.v1

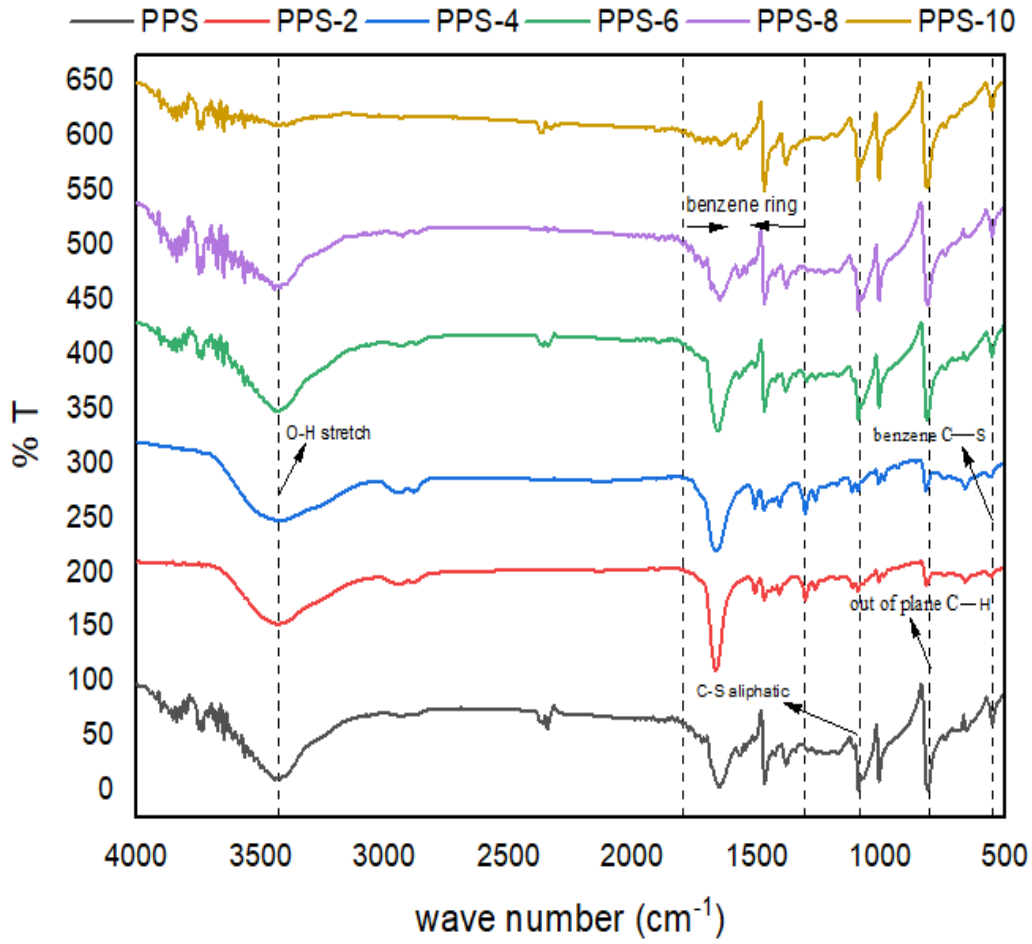

Figure 6. FTIR spectra of PPS@BC nanocomposites.

The characteristic C-S aliphatic stretching vibrations of the benzene ring are assumed to be present at 1084 to 1089 cm^{-1}. This aliphatic C-S bond is present at a higher frequency than the C-S bond due to the benzene ring. This trend is obvious due to the restricted movement of sulfur attached to the carbon of the benzene ring. The electronic cloud of the diffused benzene ring has lowered the movement of adjacent bulky sulfur atom of the polymer backbone. There is present a noticeable peak at 3433 cm^{-1} which is due to the formation of an additional O-H bond. This bond was absent in neat polymer. It is assumed that these O-H bonds are created during the coagulation process where methanol was used as a coagulant. During the sonication of methanol with the polymer skeleton there occurred some productive interaction which created polar bonds on the PPS matrix. The intensity of this bond increases with the increase of filler content up to 4 % addition after this intensity of the O-H bond is decreased again. This indicated the fact that an extra quantity of filler will hinder the beneficial interaction of methanol with polymer skeleton. This increase in the polar character of the polymer matrix will incorporate strong intermolecular forces, which can be beneficial for improving the mechanical, thermal, and surface-related properties of the synthesized nanocomposite.

4.5. Thermogravimetric analysis of PPS@BC nanocomposite

Thermograms of neat PPS and PPS@BC nanocomposites are presented in Figure 7. The detail of the data is listed in Table 6. The thermal stability of the nanocomposites is predicted by using the information about the temperature at 5 % weight loss (T_5), the temperature at 10% weight loss (T_{10}), the temperature at 50 % weight loss (T_{50}), the final degradation temperature (T_f), and residual weight at T_f (R_f). All the PPS@BC nanocomposites along with neat PPS are degraded above 640 °C. The

Preprints (www.preprints.org) | NOT PEER-REVIEWED | Posted: 16 March 2023 doi:10.20944/preprints202303.0303.v1

addition of 6 % BC has resulted in the rise of 13 ˚C in T_f compared with neat polymer. Suggesting that the nanocomposite can be applied at a somewhat higher temperature. 5 % and 10 % weight loss temperature is found maximum for PPS-6 suggesting its initial weight loss will take place at a higher temperature.

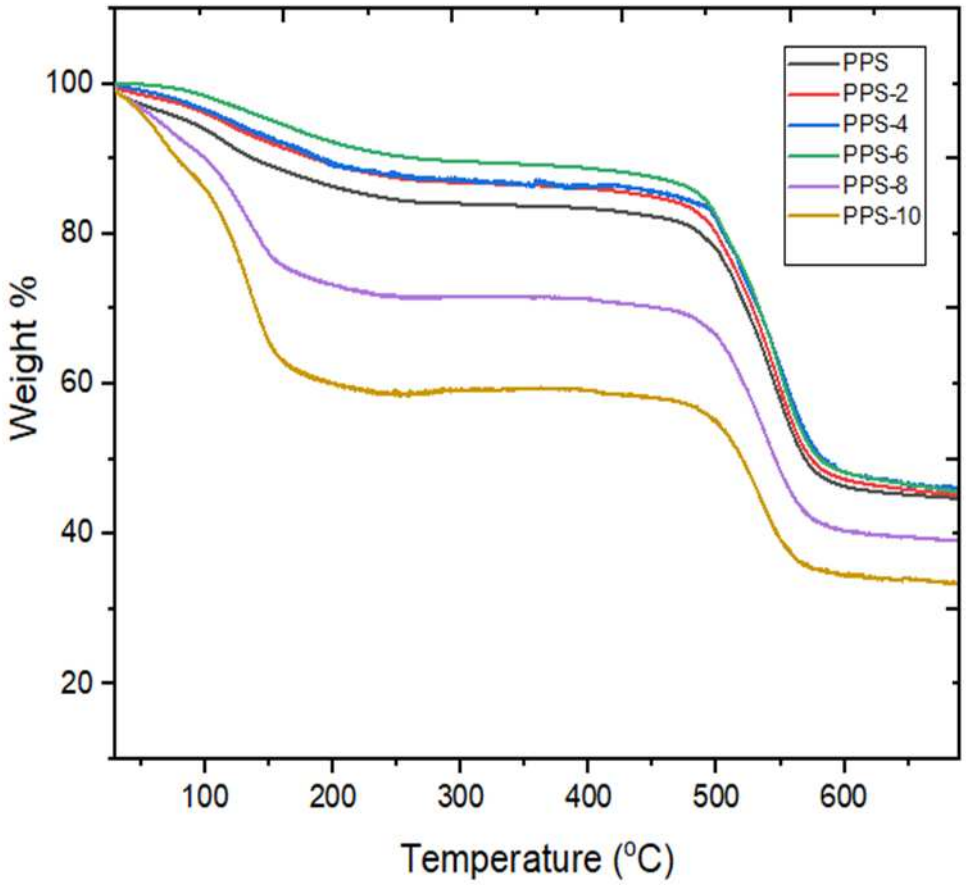

Figure 7. TGA curves of PPS@BC nanocomposites.

Table 6. TGA data of PPS@BC nanocomposites.

Compounds	T_5 (°C)	T_{10} (°C)	T_{50} (°C)	T_f (°C)	R_f (%)
PPS	90	127	567	646	45
PPS-2	118	187	573	654	46
PPS-4	123	188	579	656	46
PPS-6	157	250	580	659	46
PPS-8	66	100	545	645	39
PPS-10	56	76	521	606	34

The increase in thermal stability from 90 ˚C to 157 ˚C is noticed while raising the filler content from 2 to 6%. Half weight loss temperature of nanocomposites ranges from 520-580 ˚C for all the prepared nanocomposites. It is evident from thermograms that for the 2 to 4 percent loading of filler into PPS the nanocomposites are showing comparable thermograms. For the nanocomposites having 8 and 10 percent filler content, there is a drastic decline in T_5, T_{10}, and T_{50}. This indicates the fact that with greater loading of the filler initial weight loss will take place at low temperatures this may be due to the easy residual solvent loss for composites with higher filler content. The residual weight (R_f) is calculated to be the same for 2 to 6 % filler content and the lowest residual weight is observed

Preprints (www.preprints.org) | NOT PEER-REVIEWED | Posted: 16 March 2023 doi:10.20944/preprints202303.0303.v1

for 10 % loading of nanocarbon. It is concluded that mixing 6 % of the synthesized nanocarbon obtained from the coconut shell into PPS is the optimum concentration that can be utilized. Its final degradation is happening at 13 ˚C higher than neat PPS which suggests that the presence of nanocarbon prepared from coconut shell has delayed the oxidative degradation of PPS. The comparative illustration of all the samples for thermal stability is presented in Figure 8.

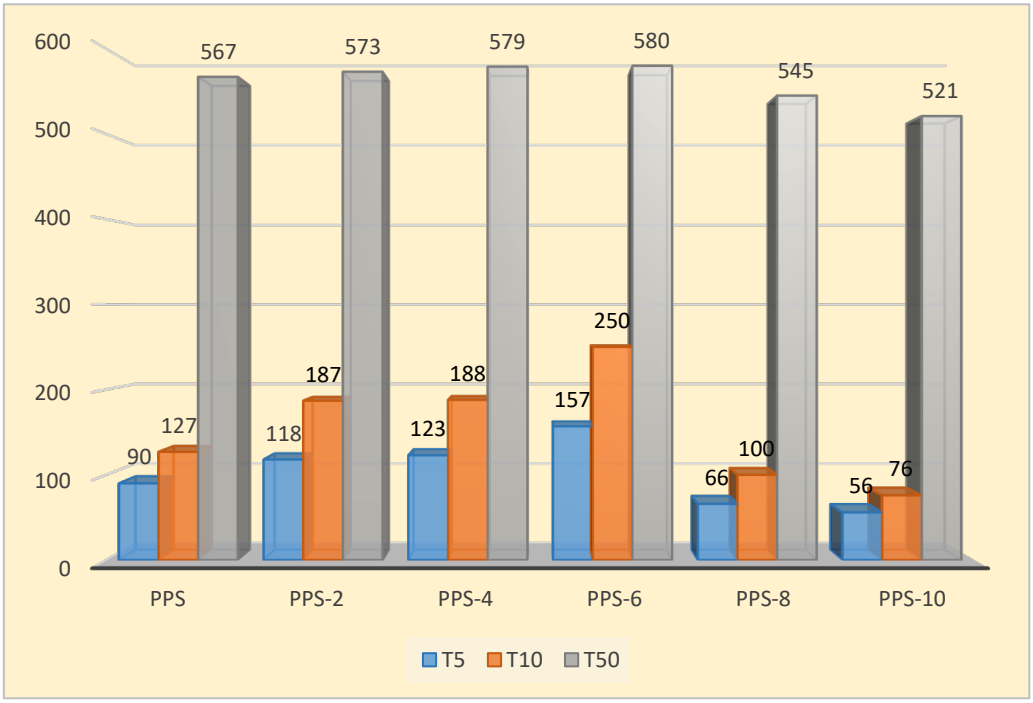

Figure 8. Comparative analysis T_5, T_{10}, and T_{50} PPS@BC nanocomposites.

4.6. Differential scanning calorimetric investigation of PPS@BC nanocomposite

Literature reveals the modification of thermoplastic material results in the variation in crystallinity behavior [50]. These crystallinity changes can be utilized to study the effect on mechanical characteristics. DSC analysis provides an indirect path to calculate the degree of crystallinity and glass transition temperature of polymer composites. DSC curves of the PPS and coagulation processed PPS/BC nanocomposite were studied over the temperature range of -50°C to 350°C. The DSC results for melting and cooling cycles are displayed in Figure 9. All samples showed an endothermic melting peak with variation in values of cooling temperature (T_c), melting temperature (T_m), Heat developed during cold crystallization ΔH_c, Heat absorbed during melting (ΔH_m), degree of supercooling ΔT (T_m - T_c), degree of crystallinity (X_c), and glass transition temperature (T_g).

All the thermal parameters for crystallization and melting behavior are listed in Table 7. The results are tabulated from the heating-cooling-heating scans of PPS@BC nanocomposites. The degree of crystallinity was calculated from equation (2) [51]:

$$\% Xc = \frac{\Delta Hc}{\Delta Hf - (1 - Wf)} * 100 \quad (2)$$

where X_c = degree of crystallinity

ΔH_c = heat of crystallization

ΔH_f = heat of crystallization of a 100% crystalline PPS, 112 J/g [52].

W_f = weight fraction of BC content in the nanocomposite.

It was revealed that adding BC nanofiller has increased the onset temperature of crystallization (T_{oc}) and crystallization temperature (T_c) of PPS@BC nanocomposites as compared to neat PPS. With the gradual addition of filler maximum attainable value of T_c is 258 °C for the selected series of the nanocomposite. The onset temperature of melting (T_{om}) and melting temperature (T_m) of PPS@BC nanocomposites also revealed the same trend of increase in value. The maximum achievable value is

Preprints (www.preprints.org) | NOT PEER-REVIEWED | Posted: 16 March 2023 doi:10.20944/preprints202303.0303.v1

284 °C for nanocomposite having 6 % filler content. The graphic evaluation of T_m and T_c for PPS and PPS@BC nanocomposites is presented in Figure 10.

From the DSC trace of the cooling cycle, it is evidenced that the crystallization process of PPS has been accelerated by the addition of filler, as there is a narrowing of the crystallization peak. The degree of supercooling (Δ) in Figure 11 shows a decrease in value compared with that used for required for the PPS crystallization in the composites was lower compared with that required for neat PPS. The drop in value of the degree of supercooling indicated that the nucleation process has been enhanced due to the presence of the BC nanofiller.

Table 7. Data obtained from DSC trace of PPS@BC nanocomposites.

Compounds	T_{oc} (°C)	T_c (°C)	ΔH_c (J/g)	T_{om} (°C)	T_m (°C)	ΔH_m (J/g)	ΔT (°C)	X_c (%)	T_g (°C)
PPS	252.1	242.5	45.2	261.7	281.8	35.9	38.5	40.4	134.7
PPS-2	265.2	257.4	41.6	271.6	284.8	29.2	27.4	37.89	129.6
PPS-4	264.8	256.9	35.8	263.4	284.5	28.6	27.5	34.7	119.4
PPS-6	269.5	258.3	36.0	274.5	284.8	12.0	26.5	33.5	117.5
PPS-8	268.4	255.1	25.7	265.6	283.9	28.6	28.8	24.4	135.4
PPS-10	269.5	253.2	22.7	268.8	283.9	16.7	30.6	22.5	149.8

The degree of crystallization showed a continuous decrease of up 16 % with the addition of filler. The glass transition temperature showed a first decline in value till PPS-6 and again a rise in parameter till PPS-10. The glass transition curves are presented in Figure 12. As the nanocomposites having lower glass transition values are easy to undergo molding, only 6 % doping with filler is found feasible to have a nanocomposite with a 17 °C lower glass transition temperature than PPS. The comparative evaluation of the degree of crystallinity and glass transition temperature of each sample is presented in Figure 13.

The PPS@BC nanocomposite blends showed two separate peaks for the melting and crystallization process. The heat of crystallization of PPS@BC nanocomposites was observed to increase continuously with an increase in dopant content. This indicated the supportive role of BC in the crystallization step during mixing via coagulation. The temperature of onset of crystallization of PPS is moved to a higher value on PPS@BC nanocomposites whereas the temperature of onset of melting showed a comparatively smaller rise in value as presented in Figure 10. The rise in temperature of crystallization of PPS predicts improved nucleation with the blending of prepared BC. It was evidenced that a 6 % addition of BC has contributed maximum towards the increase of crystallization rate.

4.7. Surface morphology and composition of PPS@BC

The FESEM imaging results of the PPS@BC nanocomposite and neat PPS using various resolutions are produced in Figure 13. All images reveal less agglomeration, good blending, and uniform dispersion of BNC in the PPS matrix. These parameters are required for better mechanical properties (such as fracture resistance, tensile strength, and elongation at the break) of nanocomposites. Morphology of the neat resin of PPS was noted with an elongated crack appearance on the bulky structure. Nanocomposites revealed the conversion of PPS morphology into a fine-grained structure with reduced surface cracks and roughness. This ensured the productive interaction of synthesized BC into

Preprints (www.preprints.org) | NOT PEER-REVIEWED | Posted: 16 March 2023 doi:10.20944/preprints202303.0303.v1

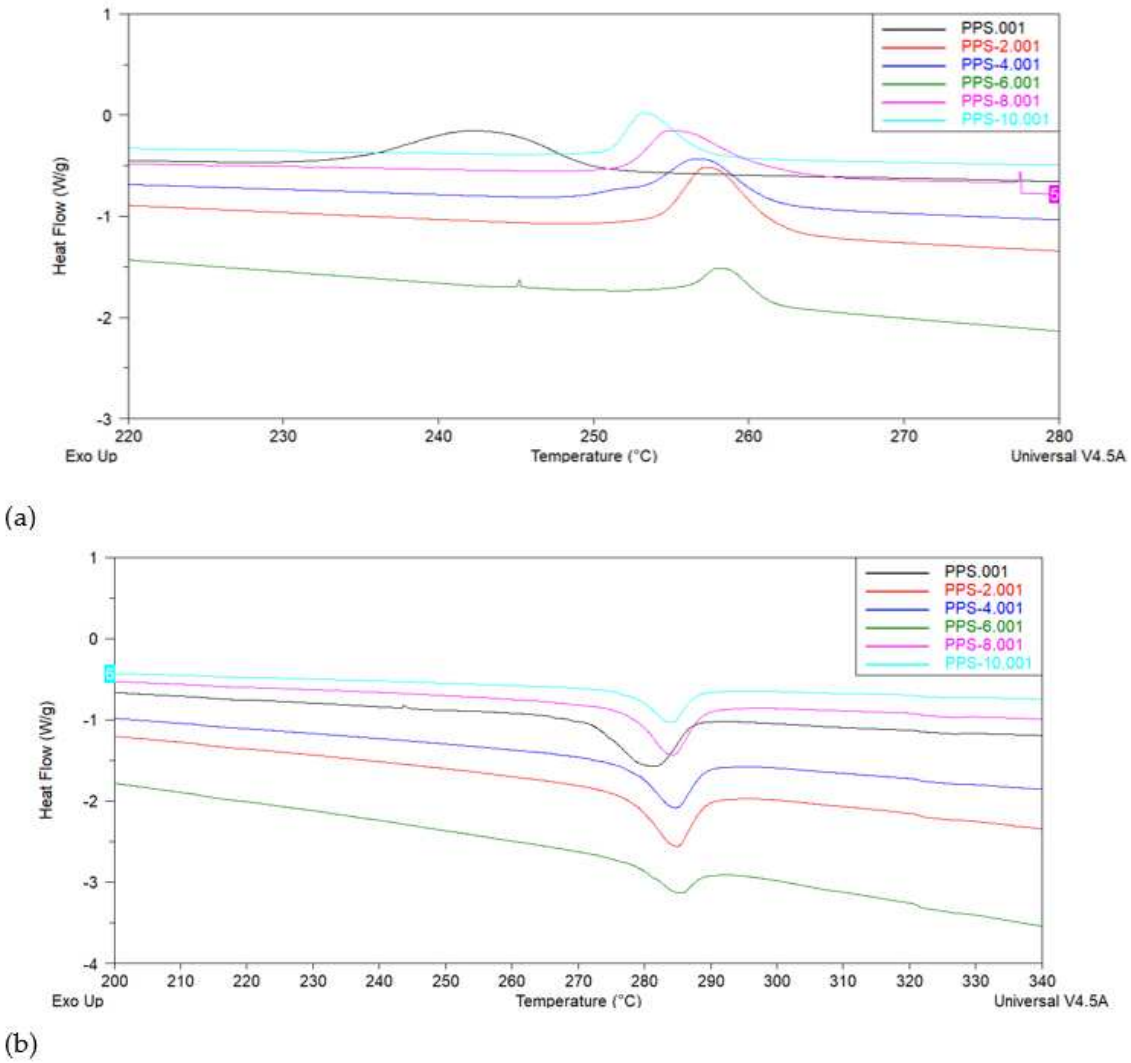

Figure 9. DSC curves of PPS@BC nanocomposites (a) cooling cycle (b) heating cycle.

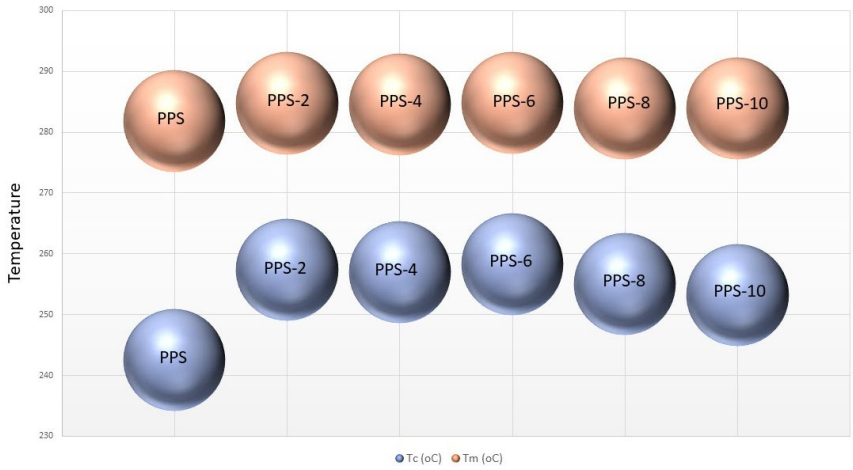

Figure 10. Comparative illustration of T_c and T_m of PPS@BC nanocomposites.

Preprints (www.preprints.org) | NOT PEER-REVIEWED | Posted: 16 March 2023 doi:10.20944/preprints202303.0303.v1

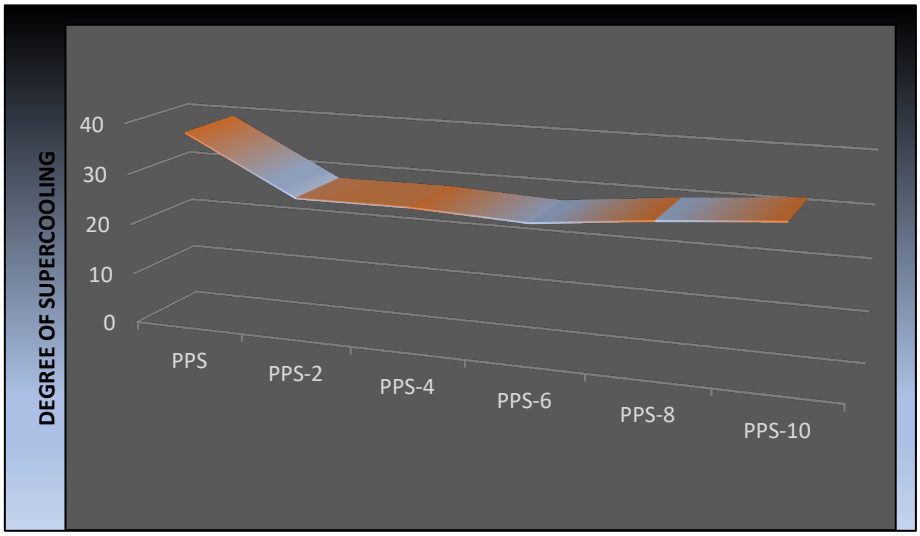

Figure 11. Graphic illustration of the change in the degree of supercooling of PPS@BC nanocomposites.

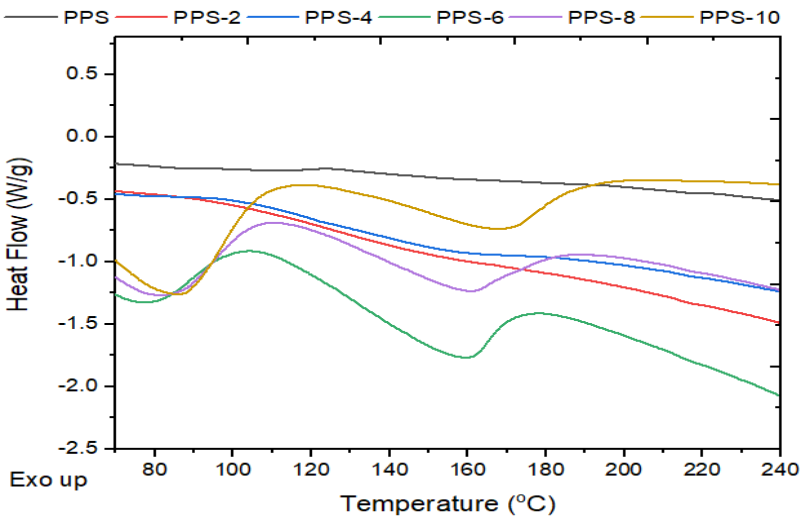

Figure 12. Glass transition analysis of PPS@BC nanocomposites.

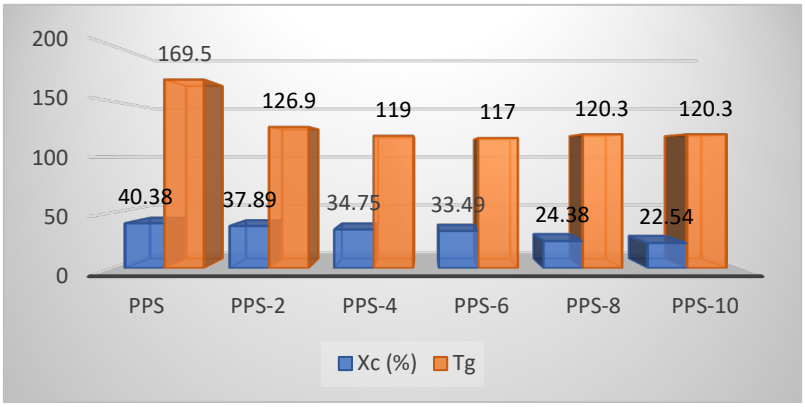

Figure 13. Comparison of the degree of crystallinity and glass transition temperature of PPS@BC nanocomposites.

Preprints (www.preprints.org) | NOT PEER-REVIEWED | Posted: 16 March 2023 doi:10.20944/preprints202303.0303.v1

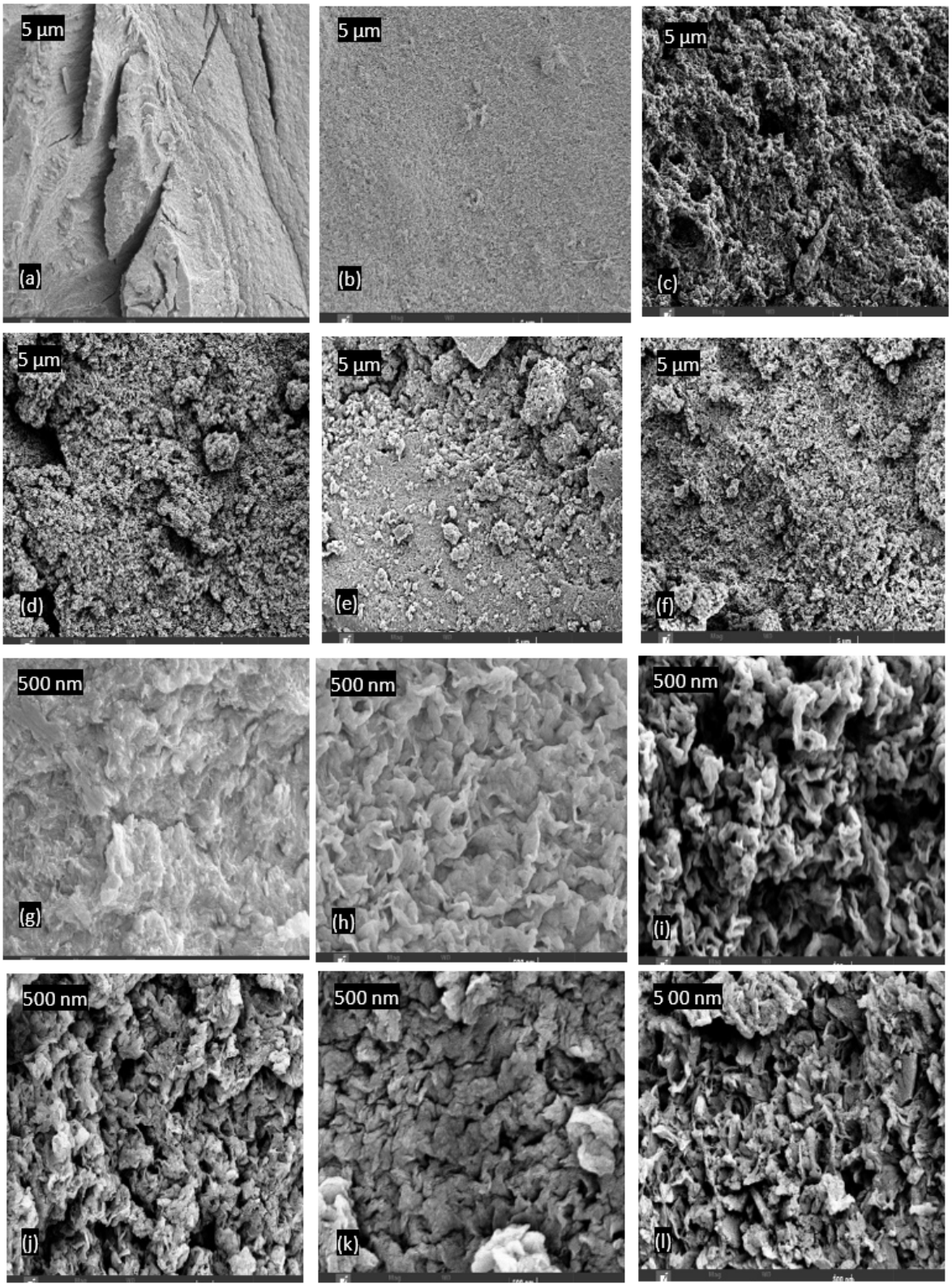

Figure 13. FESEM images of samples (a) PPS at 5 µm (b) PPS-2 at 5 µm (c) PPS-4 at 5 µm (d) PPS-6 at 5 µm (e) PPS-8 at 5 µm (f) PPS-10 at 5 µm (g) PPS at 500 nm (h) PPS-2 at 500 nm (i) PPS-4 at 500 nm (j) PPS-6 at 500 nm (k) PPS-8 at 500 nm (l) PPS-10 at 500 nm.

Preprints (www.preprints.org) | NOT PEER-REVIEWED | Posted: 16 March 2023 doi:10.20944/preprints202303.0303.v1

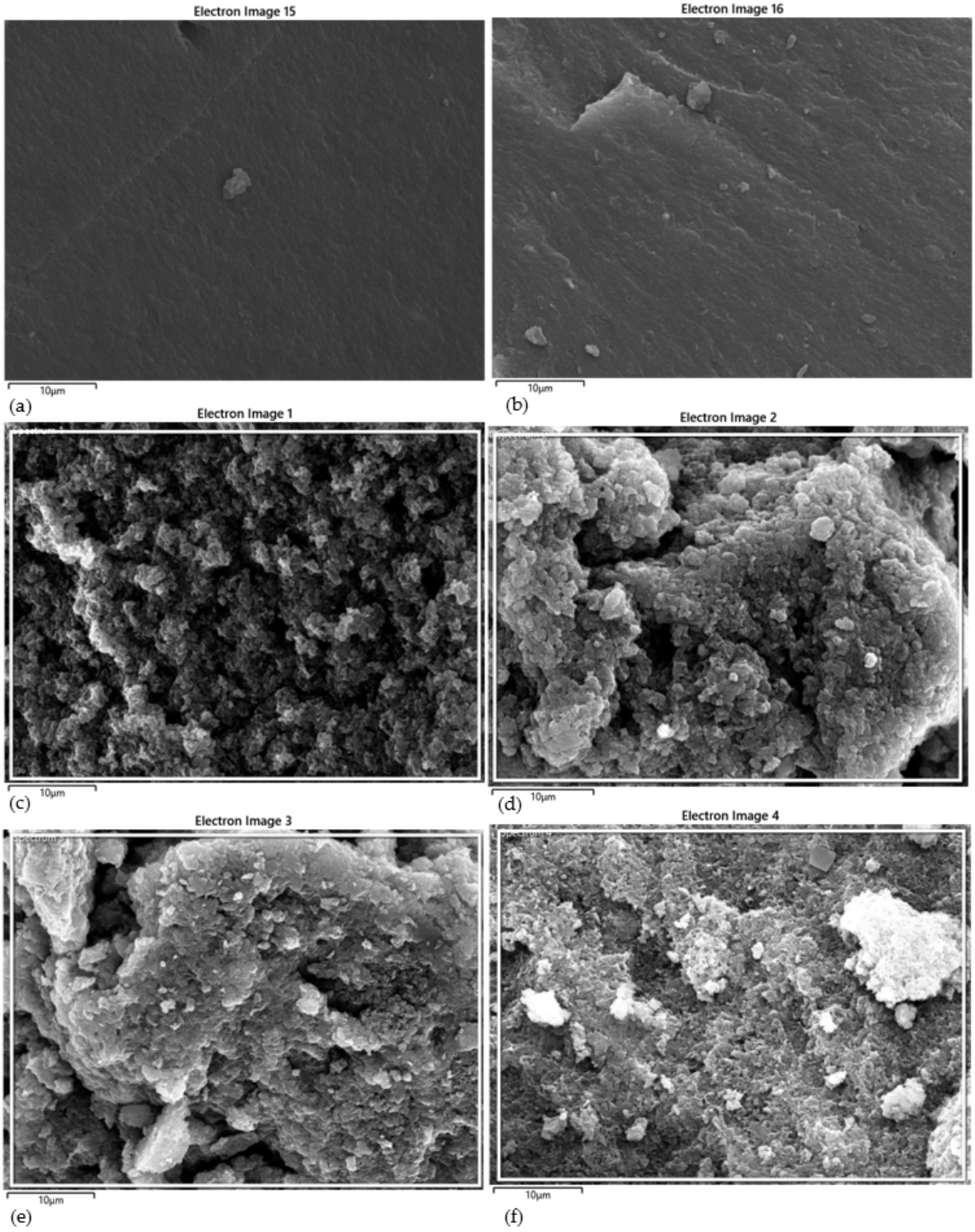

Figure 14. BSE images of PPS@ BC nanocomposites (a) PPS, (b) BSE PPS-2, (c) PPS-4, (d) PPS-6, (e) PPS-8, (f) PPS-10.

Preprints (www.preprints.org) | NOT PEER-REVIEWED | Posted: 16 March 2023 doi:10.20944/preprints202303.0303.v1

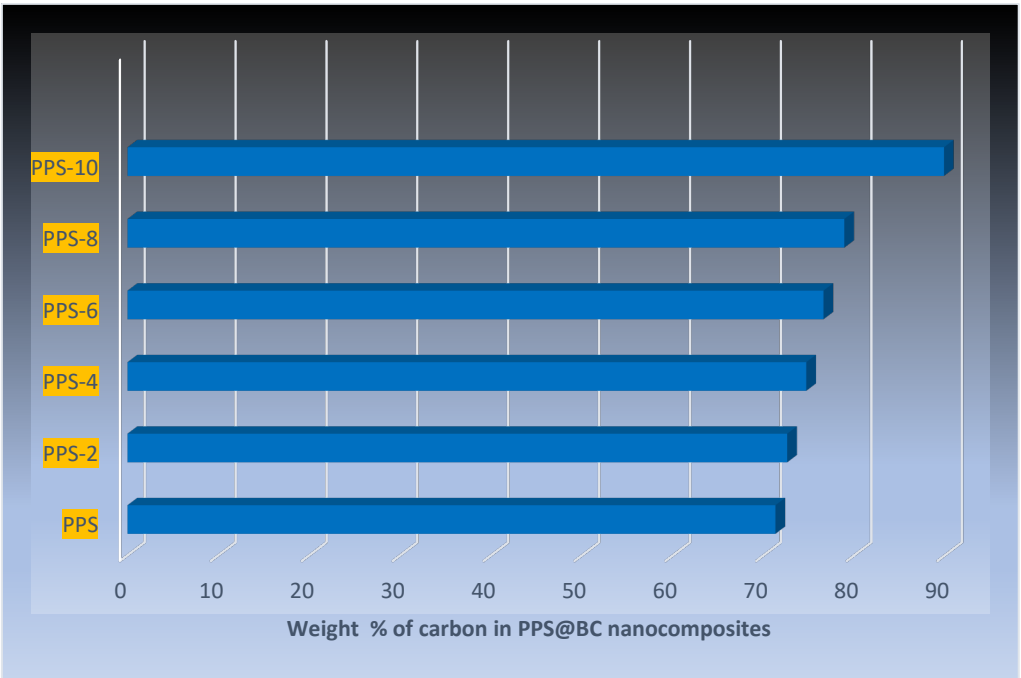

Figure 15. Quantitative analysis results of weight fraction of carbon from EDS.

the polymer during coagulation. The filler used as a dopant is observed to have good penetration into the inter-spherulitic and interlamellar regions of PPS chains [53,54]. The diffusion of BC remains homogenous even after an increase in dopant concentration. This rapid diffusion is possibly due to chaos in crystallite structure during the coagulation process. During composite formation, the change in morphology of the inner structure of the polymer skeleton with the creation of voids throughout the cross section is noticed.

There are distinguishing features like interior voids and continuous saturation of BC nanoparticles into the polymeric matrix. No evidence of aggregation of BC has been perceived, indicating a supportive role of the coagulation method in wetting the PPS resin with filler. Carbon-based fillers are reported to increase the porosity of polymer nanocomposites due to higher surface area [53]. The detailed morphological images obtained by EDS are given as BSE (backscattered electron) images in Figure 14. These in-depth images also correlate in surface morphology with FESEM images. The results of the weight fraction of carbon in prepared nanocomposites are given in Figure 15. This also indicated the increase in carbon content with the addition of BC.

5. Conclusions

The mesoporous BC synthesized using the facile carbonization step has an effective surface area and crystallinity to be used as filler. Its effective dispersion into PPS@BC nanocomposites was achieved by using a simple coagulation technique. The BC has displayed a role in increasing the thermal stability of nanocomposite. The crystallization process of PPS nanocomposite was boosted and the flexibility of the polymer due to the decline in crystallinity is improved when related to neat PPS. In polymer nanocomposites, the filler is known to control the morphology, crystallization, and nucleation process. The polymer nanocomposites showed improved crystallinity and glass transition temperature values compared with PPS resin. The appearance of a rubbery trend in the glass transition peak with a decline in value up to 6% filler mixing is indicative of ease of molding due to the introduction of the amorphous character. The melting temperature and crystallization temperature were slightly affected by the change in filler content. A rise in heat of crystallization in PPS@BC nanocomposite indicates ease in the crystallization process as a result of blending through coagulation. With the increase in the percentage of BC, beyond 6% the crystallization of the PPS skeleton was disturbed and a decrease in the crystallinity index was noted. The rise in amorphous

character is directly associated with easy crosslinking of the polymer chain. The melting temperature and crystallization temperature were slightly affected by the change in filler content. A rise in heat of crystallization in PPS@BC nanocomposite indicates ease in the crystallization process as a result of blending through coagulation. The rise in lowest glass transition temperature after was also noticed with 6 % BC loading is indicative of hindering of excessive filler quantity in effective overlapping of the polymer chains mixing. These properties predict the usage of synthesized nanocomposites in chemical processing industries for surface applications involving the coating of thread guides, molds, casings, driers, and valves.

Acknowledgments: The authors would like to greatly acknowledge the Department of Fundamental and Applied Sciences, Universiti Teknologi PETRONAS (UTP) for its support.

CONFLICTS OF INTEREST: The authors declare no conflict of interest.

References

1. L. A. Wilke, C. G. Robertson, D. A. Karsten, and N. J. Hardman, "Detailed understanding of the carbon black–polymer interface in filled rubber composites," *Carbon,* vol. 201, pp. 520-528, 2023.
2. S. Ayub, B. H. Guan, and F. Ahmad, "Graphene and Iron based composites as EMI shielding: A Systematic Review," in *2020 Second International Sustainability and Resilience Conference: Technology and Innovation in Building Designs (51154)*, 2020: IEEE, pp. 1-5.
3. S. Ayub *et al.*, "Graphene and iron reinforced polymer composite electromagnetic shielding applications: A review," *Polymers,* vol. 13, no. 15, p. 2580, 2021.
4. Y. Nezili *et al.*, "Solvent polarity impacts the sorption kinetics and tensile properties of carbon black filled elastomers," *Polymer,* vol. 264, p. 125563, 2023.
5. K. Zadafiya, D. Bandhu, S. Kumari, S. Chatterjee, and K. Abhishek, "Recent trends in drilling of carbon fiber reinforced polymers (CFRPs): A state-of-the-art review," *Journal of Manufacturing Processes,* vol. 69, pp. 47-68, 2021.
6. S. Ayub, B. H. Guan, F. Ahmad, M. F. Javed, A. Mosavi, and I. Felde, "Preparation Methods for Graphene Metal and Polymer Based Composites for EMI Shielding Materials: State of the Art Review of the Conventional and Machine Learning Methods," *Metals,* vol. 11, no. 8, p. 1164, 2021.
7. S. Kumar, B. K. Satapathy, and A. J. C. m. s. Patnaik, "Thermo-mechanical correlations to erosion performance of short glass/carbon fiber reinforced vinyl ester resin hybrid composites," vol. 60, pp. 250-260, 2012.
8. S. Ayub, B. H. Guan, F. Ahmad, and Z. U. Nisa, "A Shear Mixing approach in Polymer Composite Formation," in *2021 Third International Sustainability and Resilience Conference: Climate Change*, 2021: IEEE, pp. 205-210.
9. S. Ayub, H. Soleimani, B. H. Guan, Z. U. Nisa, and F. Ahmad, "Graphene, Copper and Nickel based composites in EMI applications: A brief review," in *2022 International Conference on Data Analytics for Business and Industry (ICDABI)*, 2022: IEEE, pp. 525-527.
10. A. F. Boostani *et al.*, "Strengthening mechanisms of graphene sheets in aluminium matrix nanocomposites," *Materials & Design,* vol. 88, pp. 983-989, 2015.
11. P. J. A. E. M. Greil, "Perspectives of nano-carbon based engineering materials," vol. 17, no. 2, pp. 124-137, 2015.
12. C. L. M. Martinez *et al.*, "Hydrothermal carbonization of lignocellulosic agro-forest based biomass residues," vol. 147, p. 106004, 2021.
13. Z. un Nisa, L. K. Chuan, S. Ayub, B. H. Guan, and F. Ahmad, "Thermal and Morphological Characterization of Coagulation-Processed Nanocomposite of Polypropylene and Bio-nanocarbon obtained from Bamboo," in *2021 Third International Sustainability and Resilience Conference: Climate Change*, 2021: IEEE, pp. 436-439.
14. S. Ayub *et al.*, "Optimization of magnetite with modified graphene for microwave absorption properties," *Journal of Alloys and Compounds,* vol. 936, p. 168182, 2023.
15. G. J. J. o. t. S. A. I. o. M. McDougall and Metallurgy, "The physical nature and manufacture of activated carbon," vol. 91, no. 4, pp. 109-120, 1991.
16. W. M. A. W. Daud and W. S. W. J. B. t. Ali, "Comparison on pore development of activated carbon produced from palm shell and coconut shell," vol. 93, no. 1, pp. 63-69, 2004.
17. L. B. J. A. S. Khalil and Technology, "Porosity characteristics of chars derived from different lignocellulosic materials," vol. 17, no. 9, pp. 729-739, 1999.
18. S. Ayub *et al.*, "Magnetite deposit on graphene nanoplatelets Surface: An assessment of grafting parameters," *Ain Shams Engineering Journal,* vol. 14, no. 7, p. 101996, 2023.
19. V. V. Rampur, A. R. Banagar, U. Ganesh, C. Srinivas, and S. Reur, "Mechanical characterization of wood apple and coconut shell reinforced hybrid composites," in *AIP Conference Proceedings*, 2020, vol. 2247, no. 1: AIP Publishing LLC, p. 040001.

20. M. Dong *et al.*, "Thermoplastic polyurethane-carbon black nanocomposite coating: Fabrication and solid particle erosion resistance," vol. 158, pp. 381-390, 2018.
21. A. M. Diez-Pascual and M. J. P. Naffakh, "Tuning the properties of carbon fiber-reinforced poly (phenylene sulphide) laminates via incorporation of inorganic nanoparticles," vol. 53, no. 12, pp. 2369-2378, 2012.
22. H. Zhai, X. Zhou, L. Fang, and A. J. J. o. a. p. s. Lu, "Study on mechanical properties of powder impregnated glass fiber reinforced poly (phenylene sulphide) by injection molding at various temperatures," vol. 115, no. 4, pp. 2019-2027, 2010.
23. A. S. Rahate, K. R. Nemade, and S. A. Waghuley, "Polyphenylene sulfide (PPS): state of the art and applications," *Reviews in Chemical Engineering,* vol. 29, no. 6, pp. 471-489, 2013.
24. Z. U. Nisa, L. K. Chuan, B. H. Guan, S. Ayub, and F. Ahmad, "Anti-Wear and Anti-Erosive Properties of Polymers and Their Hybrid Composites: A Critical Review of Findings and Needs," vol. 12, no. 13, p. 2194, 2022. [Online]. Available: https://www.mdpi.com/2079-4991/12/13/2194.
25. B. Vieille, J. Aucher, and L. J. A. i. P. T. Taleb, "Carbon fiber fabric reinforced PPS laminates: Influence of temperature on mechanical properties and behavior," vol. 30, no. 2, pp. 80-95, 2011.
26. N. L. Batista, P. Olivier, G. Bernhart, M. C. Rezende, and E. C. Botelho, "Correlation between degree of crystallinity, morphology and mechanical properties of PPS/carbon fiber laminates," *Materials Research,* vol. 19, pp. 195-201, 2016.
27. A. Jain, J. Somberg, and N. Emami, "Development and characterization of multi-scale carbon reinforced PPS composites for tribological applications," *Lubricants,* vol. 7, no. 4, p. 34, 2019.
28. O. A. Alo, I. O. Otunniyi, and E. R. Sadiku, "Processing methods for conductive polymer composite bipolar plates: Effect on plate quality and performance," *Fuel Cells,* 2023.
29. J. Jog, V. Shingankuli, and V. J. P. Nadkarni, "Crystallization of poly (phenylene sulfide) in blends with high density polyethylene and poly (ethylene terephthalate)," vol. 34, no. 9, pp. 1966-1969, 1993.
30. M. Irfan *et al.*, "A Magnetic Nanoparticle-Doped Photopolymer for Holographic Recording," *Polymers,* vol. 14, no. 9, p. 1858, 2022.
31. M. Donohue, G. J. A. i. c. Aranovich, and i. science, "Classification of Gibbs adsorption isotherms," vol. 76, pp. 137-152, 1998.
32. R. Fallah, S. Hosseinabadi, and G. Pourtaghi, "Influence of Fe3O4 and carbon black on the enhanced electromagnetic interference (EMI) shielding effectiveness in the epoxy resin matrix," *Journal of Environmental Health Science and Engineering,* vol. 20, no. 1, pp. 113-122, 2022.
33. C. Meyer, M. Weyhe, W. Haselrieder, and A. Kwade, "Heated calendering of cathodes for lithium-ion batteries with varied carbon black and binder contents," *Energy Technology,* vol. 8, no. 2, p. 1900175, 2020.
34. D. Veeman *et al.*, "Sustainable development of carbon nanocomposites: synthesis and classification for environmental remediation," *Journal of Nanomaterials,* vol. 2021, pp. 1-21, 2021.
35. S. Khodabakhshi, P. F. Fulvio, and E. Andreoli, "Carbon black reborn: Structure and chemistry for renewable energy harnessing," *Carbon,* vol. 162, pp. 604-649, 2020.
36. K. S. Sing, F. Rouquerol, and J. Rouquerol, *Adsorption By Powders and Porous Solids: Principles, Methodology, and Applications*. Academic Press, 1999.
37. J. Cao and L. J. P. c. Chen, "Effect of thermal cycling on carbon fiber-reinforced PPS composites," vol. 26, no. 5, pp. 713-716, 2005.
38. V. Shingankuli, J. Jog, and V. J. J. o. a. p. s. Nadkarni, "Thermal and crystallization behavior of engineering polyblends. I. Glass reinforced polyphenylene sulfide with polyethylene terephthalate," vol. 36, no. 2, pp. 335-351, 1988.
39. W. Li, K. Yang, J. Peng, L. Zhang, S. Guo, and H. Xia, "Effects of carbonization temperatures on characteristics of porosity in coconut shell chars and activated carbons derived from carbonized coconut shell chars," *Industrial crops and products,* vol. 28, no. 2, pp. 190-198, 2008.
40. J. Maciá-Agulló, B. Moore, D. Cazorla-Amorós, and A. Linares-Solano, "Activation of coal tar pitch carbon fibres: Physical activation vs. chemical activation," *Carbon,* vol. 42, no. 7, pp. 1367-1370, 2004.
41. W. M. A. W. Daud, W. S. W. Ali, and M. Z. J. C. Sulaiman, "The effects of carbonization temperature on pore development in palm-shell-based activated carbon," vol. 38, no. 14, pp. 1925-1932, 2000.
42. F. J. C. Rodriguez-Reinoso and p. o. carbon, "Microporous structure of activated carbons as revealed adsorption methods," vol. 21, p. 1, 1989.
43. F. Rodriguez-Reinoso, "Controlled gasification of carbon and pore structure development," in *Fundamental issues in control of carbon gasification reactivity*: Springer, 1991, pp. 533-571.
44. A. Chauhan and P. Chauhan, "Powder XRD technique and its applications in science and technology," *J Anal Bioanal Tech,* vol. 5, no. 5, pp. 1-5, 2014.
45. D. Skoog, F. Holler, and S. Crouch, "Principles of instrumental analysis, 6th edn. Brooks," *Cole, Cengage Learning, USA,* pp. 338-373, 2007.
46. C. N. Barnakov, G. Khokhlova, V. Y. Malysheva, A. Popova, and Z. J. S. F. C. Ismagilov, "X-ray diffraction analysis of the crystal structures of different graphites," vol. 49, no. 1, pp. 25-29, 2015.

47. S. Y. Oh *et al.*, "Crystalline structure analysis of cellulose treated with sodium hydroxide and carbon dioxide by means of X-ray diffraction and FTIR spectroscopy," vol. 340, no. 15, pp. 2376-2391, 2005.
48. Y. Quan, Q. Liu, S. Zhang, and S. Zhang, "Comparison of the morphology, chemical composition and microstructure of cryptocrystalline graphite and carbon black," *Applied Surface Science,* vol. 445, pp. 335-341, 2018.
49. S.-M. Lee, S.-H. Lee, and J.-S. Roh, "Analysis of activation process of carbon black based on structural parameters obtained by XRD analysis," *Crystals,* vol. 11, no. 2, p. 153, 2021.
50. Y. Zhao, M. Xiao, S. Wang, X. Ge, and Y. Meng, "Preparation and properties of electrically conductive PPS/expanded graphite nanocomposites," *Composites science and technology,* vol. 67, no. 11-12, pp. 2528-2534, 2007.
51. J. Bai, *Advanced fibre-reinforced polymer (FRP) composites for structural applications: 1. Introduction*. Elsevier Inc. Chapters, 2013.
52. K. Stoeffler, S. Andjelic, N. Legros, J. Roberge, and S. B. Schougaard, "Polyphenylene sulfide (PPS) composites reinforced with recycled carbon fiber," *Composites Science and Technology,* vol. 84, pp. 65-71, 2013.